DOI: 10.1111/cgf.13959
Eurographics Conference on Visualization (EuroVis) 2020
M. Gleicher, T. Landesberger von Antburg, and I. Viola
(Guest Editors)

Volume 39 (2020), Number 3

Knowledge-Assisted Comparative Assessment of Breast Cancer using Dynamic Contrast-Enhanced Magnetic Resonance Imaging

K. Nie[1], P. Baltzer[2], B. Preim[1], and G. Mistelbauer[1]

[1]Department of Simulation and Graphics, Otto-von-Guericke University Magdeburg, Germany
[2]Department of Biomedical Imaging and Image-guided Therapy, Medical University of Vienna, Austria

Abstract

Breast perfusion data are dynamic medical image data that depict perfusion characteristics of the investigated tissue. These data consist of a series of static datasets that are acquired at different time points and aggregated into time intensity curves (TICs) for each voxel. The characteristics of these TICs provide important information about a lesion's composition, but their analysis is time-consuming due to their large number. Subsequently, these TICs are used to classify a lesion as benign or malignant. This lesion scoring is commonly done manually by physicians and may therefore be subject to bias. We propose an approach that addresses both of these problems by combining an automated lesion classification with a visual confirmatory analysis, especially for uncertain cases. Firstly, we cluster the TICs of a lesion using ordering points to identify the clustering structure (OPTICS) and then visualize these clusters. Together with their relative size, they are added to a library. We then model fuzzy inference rules by using the lesion's TIC clusters as antecedents and its score as consequent. Using a fuzzy scoring system, we can suggest a score for a new lesion. Secondly, to allow physicians to confirm the suggestion in uncertain cases, we display the TIC clusters together with their spatial distribution and allow them to compare two lesions side by side. With our knowledge-assisted comparative visual analysis, physicians can explore and classify breast lesions. The true positive prediction accuracy of our scoring system achieved 71.4 % in one-fold cross-validation using 14 lesions.

CCS Concepts

• ***Human-centered computing*** → *Graph drawings; Visual analytics; Information visualization;* • ***Computing methodologies*** → *Vagueness and fuzzy logic;* • ***Information systems*** → *Clustering; Digital libraries and archives;*

1. Introduction

Breast cancer is the most common female's invasive cancer, accounting for almost a quarter of cancer cases among women globally, and it is also the leading cause of cancer death among women in over 100 countries [BFS*18]. Early detection of breast cancer by screening programs is supported by most expert societies [SAea17]. Commonly used diagnostic imaging modalities are mammography and breast ultrasound [WAJ*18, Nat18]. Conventional imaging is hampered by limited sensitivity and specificity. While cancers are regularly missed in women with higher mammographic breast density, positive imaging findings require image-guided biopsy to establish a final diagnosis. Biopsies, however, are invasive, and in case of stereotactic guidance costly procedures, can further cause physical pain and psychological stress to the patient [HKvH08]. The majority of these biopsies yield benign results and are thus potentially avoidable. Therefore, an additional non-invasive imaging-based diagnostic test method, such as dynamic contrast-enhanced magnetic resonance imaging (DCE-MRI), would be welcome.

For diagnosis, radiologists need to analyze the features of lesions for understanding the severity of the pathological processes and the grade of the disease. According to the breast imaging reporting and data system (BI-RADS) [BSB*09] or Göttinger Score (*GS*) [FKG99], the disease grade can be expressed as a score, which is conducive to the understanding of physicians. With the common static imaging modalities, such as mammography and breast ultrasound, radiologists can only use the morphological characteristics of the lesion for analysis. DCE-MRI, as a dynamic modality, supplies the morphological characteristics together with the functional features of breast lesions, which not only illustrate the spatial information, such as tissue structure and vascularity, but also physiological information on perfusion and permeability characteristics [MMSJP99]. Due to characteristic differences in the net capillary diameter, vessel permeability and extracellular extravascular distribution space, DCE-MRI is able to distinguish benign from malignant lesions. Based on the characteristics of DCE-MRI, the analysis of these data is mainly focused on morphological [DGV*16, MCW*16, DVK*18], texture [ASL*11, MDvP17] and temporal features [BLA*07, BFB*09, MBB*17].

Using the temporal features to analyze breast lesions is important [RPP*20], since the perfusion of contrast agent (CA) varies depending on the tissue types contained in a lesion, the temporal dy-

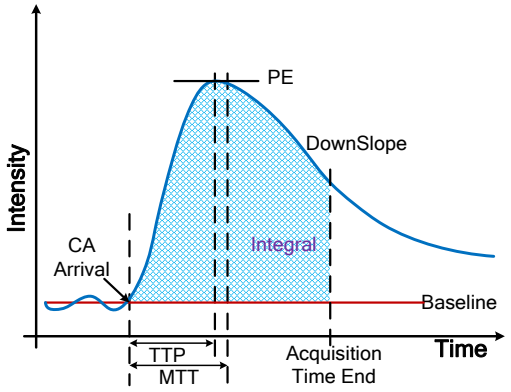

Figure 1: *A typical TIC with its parameters. PE means peak enhancement, TTP is time to peak, MTT is mean transit time, which represents the half position of the integral area. (Adapted from [POM*09])*

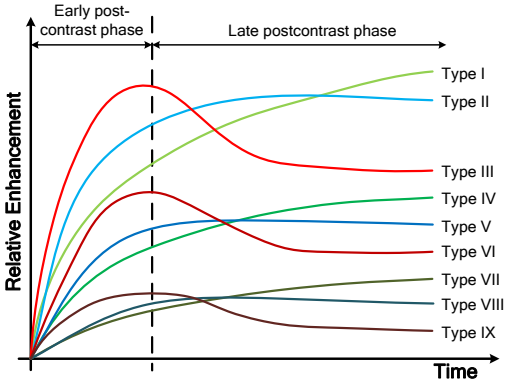

Figure 2: *Nine typical REs. At the late postcontrast phase, the curves can be divided into three categories: type I, IV, VII (*persistent*) show continuous increase, type II, V, VIII (*plateau*) reach a plateau, and type III, VI, IX (*washout*) exhibit a decreasing pattern after an initial increase. At the early postcontrast phase, the curves can also be divided into three categories: type I, II, III (*rapid*) have a rapid increase, type VI, V, VI (*normal*) increase moderately and type VII, VIII, IX (*slow*) increase slowly. (Adapted from [GPTP10])*

namics of the acquired signal, which reflects the absorption, and the release of the CA can provide a good basis for lesion classification. This temporal information can directly be expressed as the intensity change of a lesion's voxel over time, referred to as time intensity curve (TIC), which is acquired by a series of magnetic resonance imaging (MRI) scans before and after injection of CA (see Figure 1). Meanwhile, the signal intensity change percentage of a TIC can be quantified by the relative enhancement (RE) as

$$RE = 100 \cdot (I_{post} - I_{pre})/I_{pre}, \quad (1)$$

with I_{pre} being the precontrast (before CA arrival) and I_{post} being the postcontrast (after CA arrival) signal intensity [KMK*99]. Figure 2 shows the nine typical categories of RE curves [GPTP10]. Analyzing TICs and RE of a lesion allows physicians to efficiently classify it, or parts of it, as benign or malignant. Though rapid initial enhancement and distinct washout in the late phase are typical of malignant lesions, both benign and malignant lesions show variable enhancement characteristics [FGKD01, BFB*09]. To account for noise in DCE-MRI data, physicians usually select a small region of interest (ROI) instead of a single voxel and then inspect the average TIC to analyze and classify the lesion [Kuh07].

However, this approach has some limitations. It is very time-consuming and error-prone, since a vast amount of data has to be analyzed [ODH*07]. Moreover, displaying only the average TIC diminishes the dynamic characteristics of the TICs when the lesion is strongly heterogeneous, but drawing all TICs into a single plot results in overplotting. By only investigating the characteristics of TICs, the spatial information of the lesion is ignored. Recently, machine learning approaches aim to support physicians in performing this task. However, these methods are still not sufficiently accurate to cope with the large variability of the data and to compete with the diagnosis of experienced physicians [MPF*17, ZLD*19].

In this paper, we propose a knowledge-assisted visual analysis approach that allows physicians to analyze breast lesions based on the classification results of a fuzzy inference system (FIS) and then to visually confirm or correct the results. Our contributions can be summarized as:

- a visualization of TIC clusters (temporal analysis),
- a spherical histogram of TIC clusters around the lesion centroid (spatial analysis),
- a visualization of two lesions' spatio-temporal information side by side (comparative analysis),
- a fuzzy inference system for lesion scoring (classification), and
- a confirmatory visual analysis approach.

To demonstrate if the classification results of our FIS can provide physicians with a useful reference, we evaluated the classification accuracy by using one-fold cross-validation. In addition, we showed our visual analysis approach to our collaborating clinical radiologists for evaluation and feedback.

2. Related Work

Analyzing TICs to comprehend the temporal features of DCE-MRI data is widely adopted by physicians to distinguish between benign and malignant lesions [POM*09]. In order to assess breast lesions by using TICs, physicians have to detect or segment the lesions first. Traditional approaches include manual selection [ARE*14] or semi-automated [PMW*14] selection of ROIs, which contain either a part or the whole lesion. Graph cut algorithms are commonly used for segmenting lesions in medical imaging [CNZ*12]. An improved version of graph cuts is GrabCut [TGVB13], which introduces a global optimization term to calculate the link strength between vertices to improve computation efficiency and simplify implementation.

Lesions, especially malignant ones, usually contain a large number of voxels [HHHV01]. Displaying the TICs of each voxel of

such a lesion results in overplotting. To assess the major characteristics of many TICs, functional boxplots [SG11] abstract a series of curves into a representative curve and their band depth. Clustering may restrict the analysis of TICs to few cluster representatives. Iorio et al. [IFDS16] proposed a parsimonious time series clustering method with a penalized spline (P-spline) and k-means algorithm, which shows a good performance on multidimensional data measurements, while the cluster number needs to be set manually. Unlike methods that require specifying the number of clusters, such as k-means, density-based clustering methods determine the number of clusters automatically. Density-based spatial clustering of applications with noise (DBSCAN) is one of the most common density-based clustering algorithms [BK07]. Ordering points to identify the clustering structure (OPTICS) is more robust against noise compared to DBSCAN, but is more time-consuming [KKSZ11]. Patwary et al. [PPA*13] proposed a parallel implementation of OPTICS, which significantly improved the computing time.

Since spatial information is not considered when analyzing TICs, Glaßer et al. [GPTP10] proposed a visual analytics approach that merged the voxels with similar TIC perfusion parameters into the same color and glyph. This approach offers an improved TIC analysis since the spatial and temporal features are simultaneously expressed in a slice view. In a follow-up work, Glaßer et al. [GNPS13] applied density-connected subspace clustering (SUB-CLU), DBSCAN and OPTICS to cluster TICs of the most suspicious regions and displayed TICs characteristics in a slice view. This approach improves the merging accuracy of the voxels, which have similar TIC perfusion parameters. However, it cannot represent details of the dynamic characteristics of voxels in a slice view.

Machine learning approaches have recently been employed to support physicians in lesion classification. Rasti et al. [RTP17] designed a mixture ensemble of convolutional neural network models to discriminate between benign and malignant breast tumors. Zhou et al. [ZLD*19] employed 3D deep learning to classify breast lesions. Although this approach is highly accurate, it is still not comparable to experienced physicians. Besides, this approach can not provide a clear physiological interpretation of its classification model, which makes it difficult to share and reproduce the experience of physicians in this model.

Instead of a binary lesion classification, fuzzy logic can be used to model various degrees of malignancy. Furthermore, in a FIS, knowledge is represented in the form of linguistic rules. This allows physicians to share their expertise. Miranda et al. [MF15] created a breast cancer diagnosis system that is based on fuzzy logic and provides a suggestion using the BI-RADS classification. Ahadi et al. [ADL*17] introduced a fuzzy inference system to predict a benign or malignant state of a lesion, based on its physical characteristics. While these fuzzy systems employ physicians' experience and provide good classification results, they lack a feedback mechanism to take advantage of the initiative of physicians.

3. Methodology

Diagnostic visualizations play an important role in the analysis and classification of breast lesions. Manual analysis is a time-consuming process and medical visualization approaches support physicians in aggregating low-level information. Visualization and analysis techniques require additional information about the imaging data, such as the position of the lesions, their temporal intensity behavior, and the spatial distribution of TICs. Moreover, providing an estimated malignancy score based on the knowledge of experienced physicians supports guided as well as confirmatory analysis.

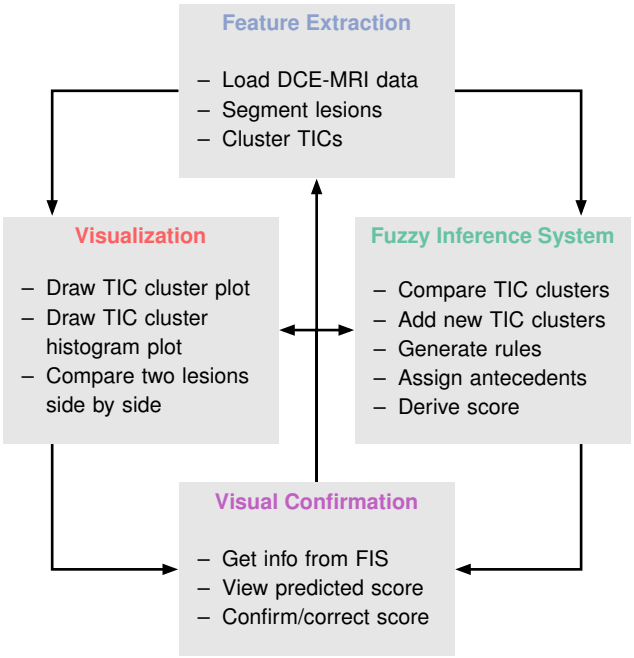

Figure 3: *Workflow of our visual analytics approach for breast lesion assessment. This approach includes four parts: feature extraction, visualization, fuzzy inference system and visual confirmation.*

The workflow of our approach is outlined in Figure 3 and consists of the following four steps: feature extraction, fuzzy inference system, visualization and visual confirmation. We first load a DCE-MRI dataset. Then, the lesions are automatically located and segmented. The TICs of the selected lesion are clustered using a parallel implementation of OPTICS clustering [PPA*13]. The feature extraction process is illustrated in Figure 4. In order to describe the spatial distribution of this lesion, we create spherical bins around it and compute a histogram of the TIC clusters. Meanwhile, a FIS is created on the basis of the TIC clusters and expert knowledge. It is used to classify lesions and predict a score. Finally, the TICs clusters and the histogram are shown to support physicians analyzing the lesion and evaluating the classification score. We also arrange both visualizations in such a way that two lesions can be compared side by side, to directly compare the current lesion with others. After the analysis, physicians can confirm the FIS score or correct it. Subsequently, we describe each step of our workflow in detail.

3.1. Feature Extraction

To extract the TICs (temporal feature) from a lesion, we establish a three-step approach (see Figure 4). All datasets were acquired over an average of 400 seconds within 11 time points and were motion-

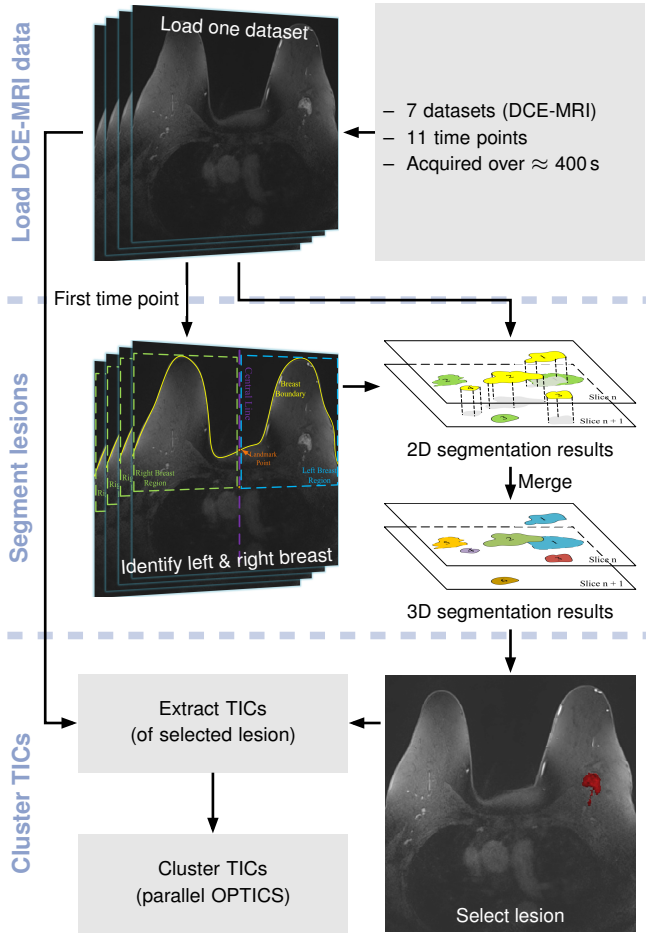

Figure 4: *Extraction of lesion features. After a DCE-MRI dataset is loaded, the images at the first time point are used to separate breast regions. With the selected dataset and the regions, suspicious objects are segmented at each slice, and then these objects are merged into 3D objects. When an object (mostly a lesion) is selected, all TICs in this object are extracted and computed to get their clusters.*

compensated afterwards. They are of resolution $384 \times 384 \times 144$ voxels. We then separate the breast regions and segment suspicious objects (including lesions and their surrounding blood vessels). The TICs of a user-selected lesion are clustered with a density-based method, which detects the number of clusters automatically.

Lesion segmentation. To facilitate physicians locating lesions and reducing the search space for subsequent image processing operations, we use the dataset of the first time point to find the breast boundary. The left and right breast are then identified by this boundary with the vertical centerline of the axial slice images. Lesions are then determined and segmented using the GrabCut [TGVB13] method. We automatically define the fore- and background seeds for GrabCut using the RE of a lesion (recall Figure 2). Since benign and malignant tumors have a rapid increase in RE at the early postcontrast phase [FGKD01], we mark such pixels inside the breast regions as foreground and pixels with slow increase in RE as background.

Compared with the conventional graph cut method [CNZ*12], GrabCut uses a new energy term to measure the L_1 distance (Manhattan distance) between the foreground and background appearance. The segmentation efficiency is optimized via this new energy term [TGVB13]. Let $S \subset \Omega$ be a segment, where S is the segmented object and Ω is the set of all image pixels. Let θ^S and $\theta^{\overline{S}}$ be the unnormalized intensity histograms for the foreground and background appearance, respectively. The energy function with the new term to consider the L_1 distance is written as follows [TGVB13]:

$$E_{L_1}(\theta^S, \theta^{\overline{S}}) = -\|\theta^S - \theta^{\overline{S}}\|_{L_1}. \tag{2}$$

Let n_k be the number of pixels in the image that belongs to bin k and let n_k^S and $n_k^{\overline{S}}$ be the number of foreground and background pixels in bin k, then Equation 2 can be rewritten as:

$$E_{L_1}(\theta^S, \theta^{\overline{S}}) = \sum_{k=1}^{K} \min(n_k^S, n_k^{\overline{S}}) - \frac{|\Omega|}{2}. \tag{3}$$

Then, K auxiliary nodes $A_1, A_2, \ldots, A_K$ are added to the graph and all pixels of bin k are connected to auxiliary node A_k. Hence, any cut separating the fore- and background pixels must either cut n_k^S or $n_k^{\overline{S}}$ number of links that connect the pixels in bin k to the auxiliary node A_k [TGVB13].

Because GrabCut is a 2D segmentation algorithm, we obtain many ROIs in each axial slice of the input dataset. By comparing the area coverage of each ROI between adjacent slices, we merge overlapping ROIs into a 3D object and then get the volume of interest (VOI). Each VOI (object, which is a lesion or its surrounding blood vessels) is separated from each other by the connectivity.

TIC clustering. By observing all VOIs (objects) in the imaging data, the user can select one that is most suspected to be a lesion. After the lesion is selected, the temporal information of its voxels in DCE-MRI breast data is extracted. We fit cubic splines to the discrete time points to obtain a continuous time representation [BJGG*03]. This allows us to model even time points between the observed data.

To cluster the TICs, we use their spline coefficients and a parallel implementation of OPTICS [PPA*13]. This method requires two parameters: ε, which describes the maximum distance (radius) to consider, and *MinPts*, the number of points required to form a cluster. The parameter *MinPts* is set to 4 in our experiments, because the smallest possible region that can be segmented by our method is 4 pixels. The other parameter ε has to be manually specified, because it controls the sensitivity to noise.

The parallel implementation of OPTICS [PPA*13] is described as follows. Let $\mathcal{D}$ be a high-dimensional data point set that contains M points. The neighborhood of a point $p \in \mathcal{D}$ within a given radius ε is defined as:

$$\mathcal{N}_\varepsilon(p) = \{q \in \mathcal{D} : d(q,p) \leq \varepsilon\,,\, q \neq p\}, \tag{4}$$

with $d(q,p)$ being the Euclidean distance between points p and q. If $|\mathcal{N}_\varepsilon(p)| \geq MinPts$, the point $p \in \mathcal{D}$ is considered a *core point*. A point $q \in \mathcal{D}$ is *directly density-reachable* with $p \in \mathcal{D}$, if $q \in N_\varepsilon(p)$. The point $q \in \mathcal{D}$ is *density-reachable* if there is a chain of points $p_1, p_2, \ldots, p_n$ with $p_1 = p$, $p_n = q$, and every p_{i+1} is *directly*

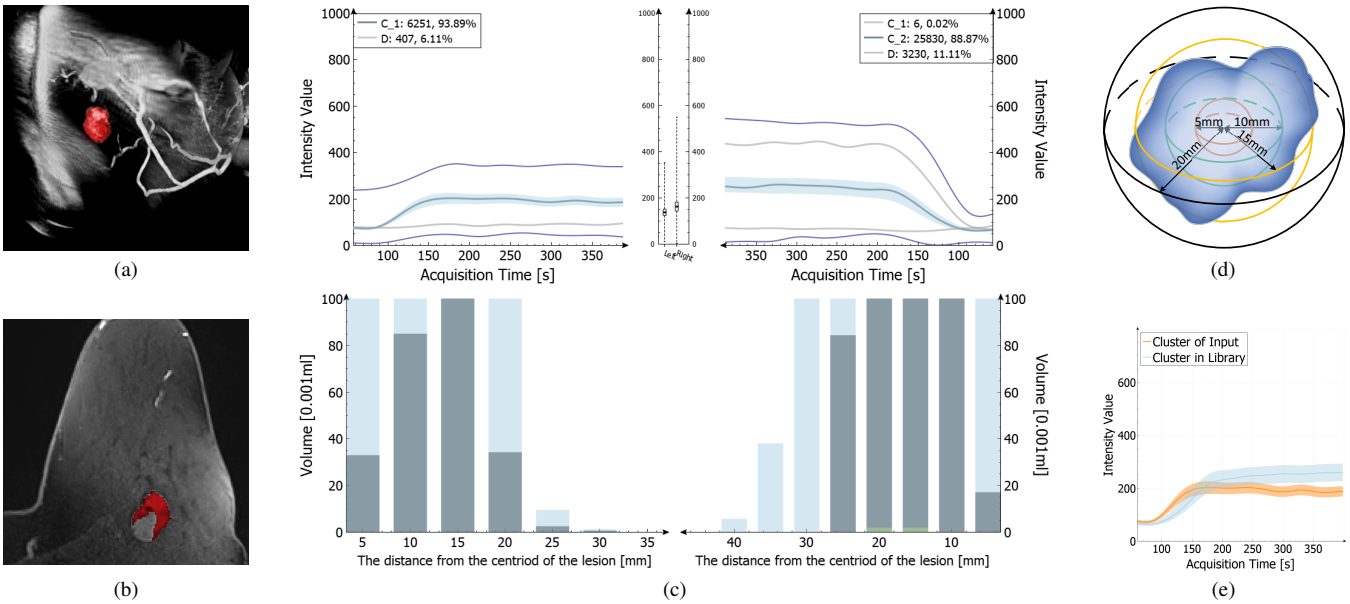

Figure 5: *Overview of our visual analysis approach. (a) shows a 3D visualization of a malignant tumor (red), whereas (b) displays an axial slice view of this tumor. The left column of (c) shows TIC clusters and their spatial distribution of a selected lesion (which is displayed in (a) and (b)). The TIC clusters and their spatial distribution in the right column of (c) are belonging to a lesion to be compared with the selected one. The middle column of (c) (between the left and right cluster plot areas) shows the statistical distribution of the selected clusters. (d) illustrates the spherical histogram bins. The center of the region is the centroid of the tumor and the size of each spherical bin is five millimeters. An input cluster (orange), which is selected in the left column of (c), and its most similar cluster (blue) in the lesion and TIC cluster library (LC library) are illustrated in (e). The relative sizes of the selected lesion are* $RS(\texttt{C\_1}) = 0.939$ *and* $RS(\texttt{D}) = 0.061$.

density-reachable from p_i, where $1 \leq i < n$ and $p_i \in \mathcal{D}$. The user-specified initial distance ε is called generating distance (GD). The smallest distance δ that satisfies $\mathcal{N}_\delta(p) \geq MinPts$ is referred to as core distance (CD). If $\mathcal{N}_\varepsilon(p) < MinPts$, the CD does not exist. The reachability distance (RD) between two points is defined as:

$$RD(p,q) = \begin{cases} 0, & \text{if } \mathcal{N}_\varepsilon(p) < MinPts, \\ \max(CD(p), d(p,q)), & \text{otherwise.} \end{cases} \quad (5)$$

Unreachable voxels ($RD(p,q) = 0$) are the noise and are excluded from the clustering. The clustering is started from an unprocessed point p that satisfies $\mathcal{N}_\varepsilon(p) \geq MinPts$. We then store the pair of points (q,p) with $q \in \mathcal{N}_\varepsilon(p)$ that have the smallest $RD(p,q)$. For any δ with $RD(p,q) \leq \delta$, the points p and q are in the same cluster as long as $\mathcal{N}_\delta(p) \geq MinPts$. If $RD(p,q) > \delta$, p and q are in different clusters. Repeatedly, a point k that is closest to the previously picked core points is selected and stored until traversing all points in space.

A minimum spanning tree (MST) [Pri57] $\mathcal{T} = \{V,E\}$ is employed, where V and E denote the set of vertices and edges of graph $\mathcal{T}$, respectively. The weight in $\mathcal{T}$ is minimal and it represents the RD between two points in $\mathcal{D}$. A MST on its local dataset is computed on a single CPU core, without any communication to other MSTs. Once all local MSTs are computed, they are merged into a global MST [PPA*13]. The final result is obtained by removing any edge (q,p), where $RD(p,q) > \delta$, from the MST and returning the points in the remaining connected components as the clusters. The MSTs and connected components can be computed in parallel, increasing the clustering performance.

To obtain a robust result, we set ε in such a way that 65-70% of a lesion's TICs are clustered based on our research. At last, we use a pointwise boxplot method [SG11], which is similar to a functional boxplot but requires less computing time to calculate the median intensity values, 50% regions and an envelope which completely encloses the values represented by a cluster.

3.2. Visualization

In order to demonstrate how our system visualizes the temporal and spatial characteristics of a lesion, we selected a malignant tumor as example. Figures 5a and 5b show this tumor highlighted in red in a 3D and 2D view, respectively. Figure 5c shows the clustered TICs of the selected tumor, and the spatial distribution of these clusters. A spherical bin, which is used to calculate the spatial distribution of the TIC clusters, is shown in Figure 5d. A selected cluster (see Figure 5c, left column) and its most similar cluster in the lesion and TIC cluster library (LC library) (see Section 3.3) are shown in Figure 5e. The selected cluster is colored in orange, while its most similar cluster is colored in blue.

When a lesion is selected, all its TICs are clustered, and the *representative curves* of each cluster are plotted. If a *representative curve* is selected, its 50% region and envelope region will be shown (see Figure 5c). In this way, it is possible to prevent different clusters from visually overlapping each other. All clusters are colored based on a scheme determined with color brewer [BHH03] to prevent the adjacent colors being similar and difficult to distin-

guish. The legend in Figure 5c describes the following attributes of a cluster. The first entry shows the corresponding color of the representative curve. Secondly, the name of the cluster is given, where C stands for a normal cluster and D for a cluster that represents a necrotic region (dead tissue). The third entry is the number of voxels of the cluster and the last entry describes the relative size in comparison to the size of all TIC clusters. The TICs that were classified as noise are not included in the plot. Whenever a cluster is selected, its statistical distribution is shown in the middle plot area (see Figure 5c).

To display the correlation between the TIC clusters (temporal features) and their spatial distribution (spatial features) of a lesion, we create a sphere with several bins to cover the entire lesion. The size of these spherical bins (see Figure 5d), which are constantly five millimeters wide, is plotted on the horizontal axis, and the number of the clustered voxels in each bin is plotted on the vertical axis (see Figure 5c, bottom). As shown in Figure 5c, we arrange the spherical histogram window below the TIC cluster window in order to provide users with comprehensive means to observe and analyze the TIC clusters. When comparing two lesions, the right side is vertically flipped, i.e., the x-axis goes from right to left. By arranging the windows side by side, differences and similarities between different tumors can be explored.

3.3. Fuzzy Inference System

We create an LC library (see Figure 6, left column) that stores the content (TICs, relative sizes, score) of each lesion. This library provides reference data for predicting a score and for supporting physicians to confirm the accuracy of the classification results in a knowledge-assisted analysis way (see Section 3.4). This library consists of two parts: a set of TIC clusters and a set of lesions. The contents of each cluster and lesion are saved in these two sets. The cluster content includes a unique cluster name, color and its intensity value at a given time point. The lesion content includes the lesion name, score (given by domain experts) and a set of its TIC clusters, which is a subset of the library's set of TIC clusters. This subset stores the cluster index (lesion's cluster name) and each TIC cluster's relative size.

Meanwhile, similar TIC clusters in the library's set of clusters will be merged to clearly reflect the associations between various clusters. If two lesions link with a large number of the same unique clusters, these lesions are considered as similar. To merge similar clusters, we employed the overlap coefficient between two clusters [MK16]. It is defined as:

$$V_S = \frac{|\mathcal{F}(C_i) \cap \mathcal{F}(C_j)|}{\min(|\mathcal{F}(C_i)|, |\mathcal{F}(C_j)|)}, \tag{6}$$

where $i \neq j$ and $\mathcal{F}(\cdot)$ indicates the 50% central region of a cluster. If $V_S \geq 0.8$, the cluster with the narrower central region will be merged with the other one.

When a new lesion (without a score) is put into the LC library, its score can be predicted via a FIS (see Figure 6). In the following, we explain the construction of our fuzzy model by linguistic translation, knowledge generation and prediction.

Linguistic translation. In order to use human semantic expressions to build expert knowledge in a FIS, the cluster's relative size

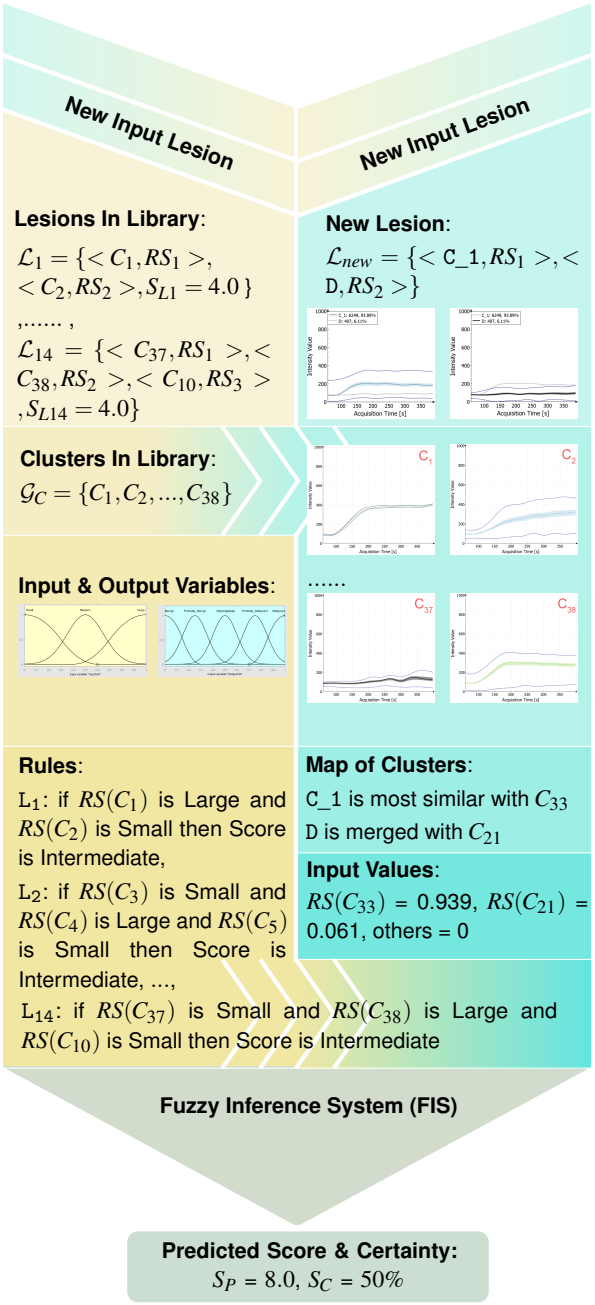

Figure 6: *Illustration of our fuzzy inference system (FIS) workflow. $\mathcal{L}_n$ are the unique lesion names, $\mathcal{G}_C$ is a set of clusters, C_n are the unique cluster names, RS is the relative size and $\texttt{L}_\texttt{n}$ is the identifier of the rules. The left column describes the structure of the LC library and the right column shows the score prediction process of a new lesion. The predicted score of the new lesion is S_P and the certainty score is S_C.*

and the lesion's score in the library should be translated into a natural language representation. The conversion of numbers to linguistic variables is defined as follows:

$$\mathsf{K}_{RS} = \begin{cases} \textit{Small}, & \text{if} \quad 0.0 \leq RS(C_n) < 0.4, \\ \textit{Medium}, & \text{if} \quad 0.4 \leq RS(C_n) \leq 0.6, \\ \textit{Large}, & \text{if} \quad 0.6 < RS(C_n) \leq 1.0. \end{cases} \tag{7}$$

$$\mathsf{K}_{S} = \begin{cases} \textit{Benign}, & \text{if} \quad 0 \leq S(\mathcal{L}_n) \leq 2, \\ \textit{ProbablyBenign}, & \text{if} \quad 2 < S(\mathcal{L}_n) \leq 3, \\ \textit{Intermediate}, & \text{if} \quad 3 < S(\mathcal{L}_n) < 5, \\ \textit{ProbablyMalignant}, & \text{if} \quad 5 \leq S(\mathcal{L}_n) < 6, \\ \textit{Malignant}, & \text{if} \quad 6 \leq S(\mathcal{L}_n) \leq 8, \end{cases} \tag{8}$$

where K_{RS} is the knowledge of relative size, K_S is the knowledge of lesion score, $RS(C_n)$ is the relative size of cluster C_n and $S(\mathcal{L}_n)$ is the score of lesion $\mathcal{L}_n$. The score of a lesion is from 0 to 8, based on *GS* [FB14], where 0 means benign and 8 malignant.

Knowledge generation. The generation of explicit knowledge is based on the lesions' contents in the library and the way humans think [FWR*17]. Knowledge is modeled in the form of linguistic rules and terms and not in the form of exact numbers when fuzzy logic is involved. These rules usually have the structure of IF-THEN clauses with their antecedents and consequents using linguistic variables and terms. The linguistic input and output fuzzy variables and their linguistic terms are shown in Figure 6. The linguistic terms *Small*, *Large*, *Medium* of the linguistic input variables are based on the sigmoid and Gaussian kernel functions, respectively. The linguistic terms *Benign* and *Malignant* of the linguistic output variables are based on the sigmoid functions, while *ProbablyBenign*, *Intermediate* and *ProbablyMalignant* use Gaussian kernel functions. The fuzzy rules K^{ε} represent the domain knowledge in a human readable form, which can be saved in an external file. This allows physicians to share and adapt their knowledge with other medical centers, which possibly increases the reproducibility of the scoring procedure. For this reason we chose a FIS, a design choice based on several discussions with one of our collaborating physicians. Some of the rules are displayed in Figure 6, where $RS(C_n)$ is the relative size of the cluster C_n in the lesion $\mathcal{L}_n$, and `Score` is the *GS* of this lesions, provided by domain experts.

Prediction. The TIC clusters `C_n` of the input lesion will be merged with the clusters C_n in the LC library. If such an input cluster cannot be merged, it is substituted with the most similar cluster from the LC library. After merging and substitution, the map of clusters and lesions will be established (see Figure 6), i. e., `C_1` $\leftarrow C_{33}$ and `D` $\leftarrow C_{21}$ with $\{$`C_1`,`D`$\} \in \mathcal{L}_{new}$ and $\{C_{33}, C_{21}\} \in$ LC library. We use the Mamdani method as inference model and the relative size of the input lesion's clusters as input values [MF15]. The schematic representation of a FIS is shown in Figure 7. For each lesion in the LC library we generate an IF-THEN rule. The antecedents of these rules consist of the LC library's clusters with their relative size and the consequents are the lesions' score. The input variables of the rules are the LC library's clusters. For each input variable, we use the relative size of the input lesion's clusters if the cluster in the LC library is merged or substituted with the one of the input lesion's clusters. If the cluster is not included in the input lesion, its relative size is zero. All implications (IF-THEN rules) are subsequently evaluated, their results aggregated using the maximum operator and then defuzzified with the centroid method [ADL*17]. The certainty

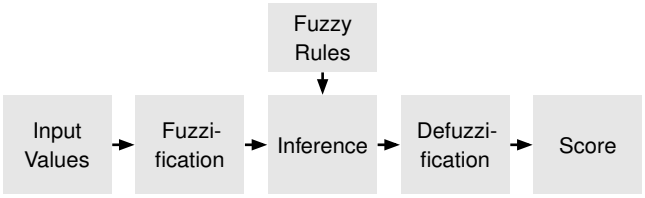

Figure 7: *Illustration of our fuzzy inference system for breast lesion classification.*

score S_C is defined as $S_C = 100 \cdot N_m / N_t$, where N_m is the number of the merged clusters and N_t is the total number of TIC clusters of the input lesion. When $S_C = 100\%$, all clusters were merged with the clusters in the LC library. This represents a certain result, because the predicted score is derived from existing knowledge. If no cluster could be merged, i.e., all were substituted, $S_C = 0\%$. It is especially important to show such results to the physicians, as they are reminded to validate the result by comparing the input lesion with several known lesions. This can be done by visually comparing lesions side by side.

3.4. Visual Confirmation

After getting the classification result (score) of a lesion from our FIS, physicians can confirm this result or correct it. If one input TIC cluster is selected, its merged or substituted cluster in the LC library is automatically found and highlighted. Meanwhile, these two clusters will be plotted simultaneously in the same area for visual verification (recall Figure 5e). If the input cluster is substituted then it will be colored in orange, otherwise, the input cluster will be red if it is merged. All clusters in the LC library can be selected for visual comparison with the input TIC cluster, which supports this verification step. The library also assists physicians in their decision-making by allowing them to examine the fuzzy rule of a lesion together with their relative sizes of the TIC clusters (IF-THEN antecedent). By comparing the spatio-temporal information of the selected lesion with a known lesion, the classification result (score, IF-THEN consequent) can be further confirmed. If the physicians think the result is wrong, they can replace the suggested score by the result obtained from analyzing the lesion using the visual analysis approach that we provide.

4. Implementation

We implemented the segmentation method, clustering, visualization, fuzzy inference system and the knowledge-assisted analysis approach in C++ using OpenMP, OpenGL, FuzzyLite, Qt and QCustomPlot. We used Qt5 for the user interface and QCustomPlot for drawing the TIC plots and histograms. The parallel OPTICS clustering was implemented in C++ and parallelized with OpenMP. Volume and slice rendering was implemented in OpenGL. We used the C++ library FuzzyLite [RV18] for the FIS. All results in this work have been created on an Intel Core i7 CPU at 2.8 GHz and 32 GB system memory.

5. Results and Discussions

In this section, we demonstrate example lesions with their TIC clusters and spatial distributions, also involved with their score prediction via FIS (see Figures 8 to 10). These lesions encompass three benign and three malignant tumors, highlighted in red in the slice views. We separately specify the ε of OPTICS (see Table 1) for each lesion such that the clustered voxels cover about 65-70% of the total number of voxels in each lesion (recall Section 3).

Table 1 shows the test results of each lesion, where ID is the lesion's identifier, DataSet is the dataset that lesion belongs to, ε is the parameter for OPTICS clustering, T_S is the segmentation time, T_C is the clustering time, S_R is the real score which is given by the domain experts, S_P is the prediction score via our FIS using one-fold cross-validation, and S_C is the certainty score (recall Section 3.3).

Figure 8 presents two breast tumors, a malignant (left) and a benign (right) one. The top images show axial slices of the DCE-MRI data, with the corresponding lesion identification at the top. The malignant tumor (left) exhibits necrosis (dead tissue), as shown by its cluster representative curve (black) and its spatial distribution. Necrosis is an important indicator of malignancy. Since we use the alpha channel when filling colors, transition colors appear when histograms with different colors are overlapping, e.g., the black histogram in the left that relates to the black cluster curve is shown as ink-blue. Analyzing clusters `C_1` to `D` of the right lesion (see Figure 8, right column), we can observe a clear upward trend throughout the entire course of time, while the trend of the left lesion's cluster `C_1` remains flat after 200 seconds. The size of each cluster or lesion can be directly compared by examining the spherical histogram of both lesions. Both lesions are removed from the LC library to predict their score. The suggested *GS* are 8.0 (left) and 4.0 (right). The cluster `D` of the left lesion is merged with C_{21} in the LC library, and cluster `C_1` is substituted (cannot be merged through the similarity matching, recall Section 3.3) by C_{11} in the LC library, so the certainty score of the left lesion is 50%. For the right lesion, its clusters `C_1`, `C_2` and `C_3` are merged with C_7, C_{19} and C_{22} in the LC library, respectively, and its cluster `D` is substituted by C_{12} in the LC library, so its certainty score is 75%.

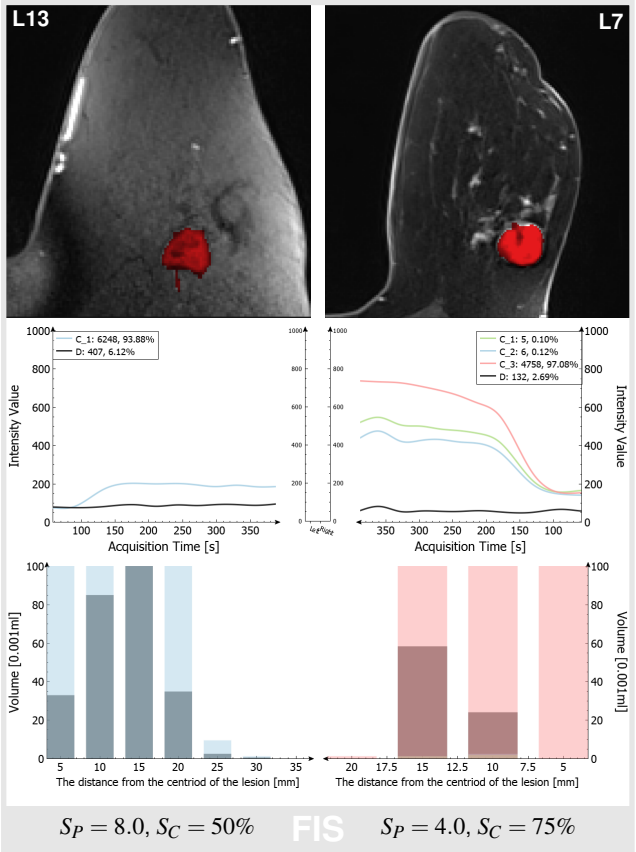

Figure 8: *Comparison of a malignant (left) and a benign (right) tumor. An axial slice view of both tumors is shown at the top. The central images show the TIC clusters and their spatial distribution is displayed below. The scores suggested by our FIS are given at the bottom together with their certainty.*

Table 1: *For each lesion we show its identifier (ID), the dataset (DataSet) it belongs to, the ε of the OPTICS clustering, the segmentation time (T_S), the clustering time (T_C), the real score (S_R), the predicted score (S_P) and the certainty score (S_C).*

ID	DataSet	ε	$T_S[s]$	$T_C[s]$	S_R	S_P	S_C
L1	D01	6.20	13.2	0.14	2	4.0	0%
L2	D02	0.93	66.5	2.17	4	4.0	100%
L3	D02	1.83	66.5	2.02	5	5.6	33%
L4	D02	0.92	66.5	2.84	5	5.6	50%
L5	D02	2.51	66.5	1.62	7	7.4	0%
L6	D03	0.92	97.3	2.43	4	4.0	50%
L7	D04	0.90	102.6	21.94	4	4.0	80%
L8	D04	0.93	102.6	39.51	7	5.0	100%
L9	D04	2.05	102.6	2.74	4	4.0	50%
L10	D04	4.09	102.6	5.32	4	6.4	33%
L11	D05	1.40	75.8	37.28	6	4.0	25%
L12	D06	0.72	131.4	510.34	8	4.0	33%
L13	D07	0.74	115.1	53.98	7	8.0	50%
L14	D07	0.50	115.1	78.73	4	4.0	33%

Two malignant lesions are compared in Figure 9. The left lesion has 2 TIC clusters of which C_1 increases slowly and then changes to a plateau. The right lesion has 4 TIC clusters with a rapid increase before 200 seconds and a slow increase thereafter. The left lesion receives a correct predicted score ($S_R : S_P = 7.0 : 7.4$) from the FIS, but the score for the right lesion is lower than the actual score given by the domain experts ($S_R : S_P = 6.0 : 4.0$). The reason for this is that the clusters `C_1` to `C_3` of the right lesion show a moderate to rapid increase and an increasing trend, making it more similar to the lower scored lesions in the LC library when used by the FIS for prediction. The rather low certainty score of the left (0%) and right (25%) lesion advises physicians to compare these lesions with several known lesions to verify their predicted score.

Two benign lesions are compared in Figure 10. TIC cluster `C_1` of the lesion shows a rapid and steady increase, whereas cluster `C_1` of the right lesion exhibits similar characteristics, but cluster `C_2` of the right lesion increases slowly and then changes to a plateau. The

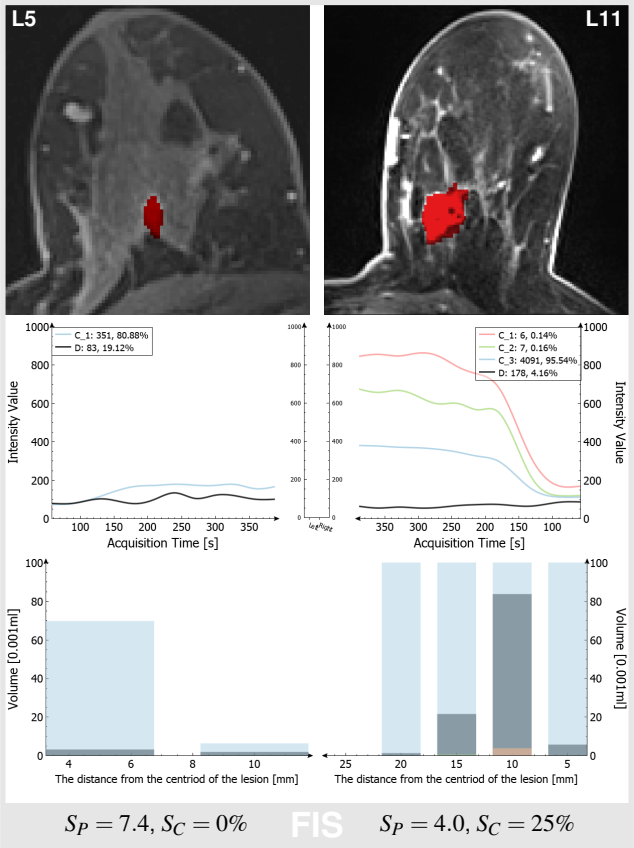

Figure 9: *Comparison of two malignant tumors. The left one gets a correct prediction score while the right one gets a wrong score.*

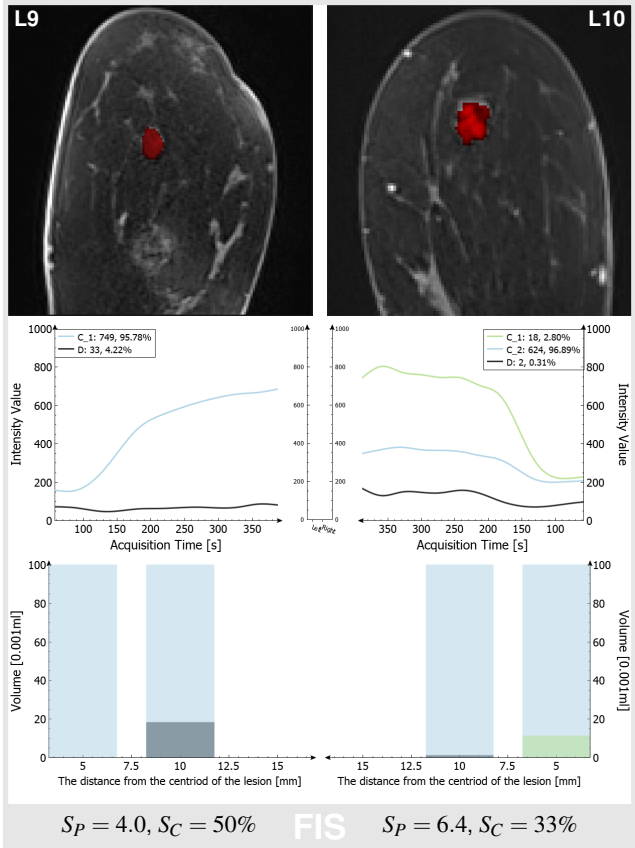

Figure 10: *Comparison of two benign tumors. The left one gets a correct prediction score while the right one gets a wrong score.*

left lesion receives a correct predicted score ($S_R : S_P = 4.0 : 4.0$) from the FIS, but the score for the right lesion is higher than the actual score given by the domain experts ($S_R : S_P = 4.0 : 6.4$). The reason for this is that the clusters `C_2` of the right lesion show a slow increase and a decrease trend after 350 seconds, making it more similar to the higher scored lesions in the LC library when used by the FIS for prediction. The certainty score of the right lesion is low (33%), physicians are advised to compare it with other known lesions to make a confident decision on the predicted score.

6. Evaluation

As shown in Table 1, lesions L2, L3, L4, L5, L6, L7, L9, L13 and L14 are accurately predicted. L1 has the lowest score and it is the only one with such a low score in our LC library. If L1 is removed from the library and a new lesion is scored by our FIS, the predicted score cannot be lower than the minimum score of the current lesions in the library, which is 4.0. Hence, we consider the predicted score of L1 to be correct, but plan to add further lesions in the future to solve this problem. The remaining incorrectly classified lesions are L8, L10, L11 and L12. Hence, our approach has a prediction accuracy of 71.4%, with 10 of 14 lesions being correctly classified.

The segmentation time T_S (see Table 1) is the time required to segment all suspicious objects (lesions and their surrounding blood vessels) in both breasts of a single dataset, and T_C is the clustering time used by the parallel OPTICS implementation. The segmentation time is mainly affected by the breast size and number of suspicious voxels, whereas the clustering time is only affected by the number of TICs in the lesion. The average segmentation and clustering time is 87.4 seconds and 54.36 seconds, respectively.

To obtain a qualitative feedback on the applicability of our visual confirmation analysis, we consulted a radiologist with three years of experience. In her opinion, the initial goal of such a tool is to speed up the workflow, reduce the interobserver variability and improve reproducibility. She also stated that *the tool seems to be quickly understood and learned by radiologists* and *it seems to be better suited for uncertain cases*. Both statements confirm our design decisions, as our tool is tailored to radiologists and uncertain cases. On the one hand, such cases are characterized by low certainty scores, and on the other hand we provide visual means to confirm or correct predicted scores. The radiologist also commented that the lesion scoring is rather subjective and our tool seems to improve the reproducibility of the scoring. This confirms the design choice of the FIS, but the radiologist mentioned that *this tool does not provide an objective score*. For this we would have to conduct a large, preferably multicenter, study. In summary, we received indicative feedback that shows the potential of our tool to deliver reproducible results. To

obtain a profound assessment of applicability and accuracy, larger and more comprehensive studies would have to be carried out.

Limitations. Although our approach automatically identifies the left and right breasts, segments and cluster lesions, and predicts the score based on FIS, it has some limitations. Firstly, the parameter ε of the clustering method has to be set manually, which means the users must have a certain understanding of the spatial distribution of the data. Secondly, our segmentation algorithm potentially removes small objects that are even difficult for experienced users to segment, especially if the lesion has only subtle changes over time. Thirdly, our analysis is currently limited to TICs and their spatial distribution, which does not involve additional spatial information, such as morphology and texture. Fourth, the number of datasets we used to construct the FIS was limited.

7. Conclusions and Future Work

We proposed a knowledge-assisted visual analysis approach that arranges the temporal and spatial characteristics of TICs side by side in order to facilitate the classification of breast lesions. By using our visual analysis approach and FIS classification result, physicians can make effective use of expert knowledge to provide a reproducible lesion score. The FIS demonstrated a good prediction accuracy, even though the number of our datasets was limited. The visual comparison of two lesions allows physicians to understand and analyze TIC clusters, which is helpful for tumor assessment. The 50% central region and the cluster envelope is only displayed for a selected cluster to avoid the mutual interference between different clusters in the same plotting area.

Future avenues are an automatic estimation of the parallel OPTICS parameter ε and the investigation of the FIS predictive power by using a larger cohort. We also plan to combine the TIC clusters with texture as well as morphological features and a profound analysis of a lesion's boundary. As suggested by one of our collaborating radiologists, we will extend the temporal and spatial TIC cluster views with a third histopathological view of a lesion and we plan to support other imaging modalities such as mammography, normal magnetic resonance imaging and ultrasound.

Acknowledgments

The authors would like to thank Joanna Rabczak, University Hospital Magdeburg, Germany, for her indispensable help and valuable feedback. The clinical data were acquired at the university hospital of Jena, Germany in a prospective, ethical review board approved (approval number 2576-06/09) study. All patients gave informed consent to the use of their anonymized MR imaging data and final diagnosis (i.e. benign vs. malignant).

References

[ADL*17] AHADI F. S., DESAI M. R., LEI C., LI Y., JIA R.: Feature-Based classification and diagnosis of breast cancer using fuzzy inference system. In *Proc. of IEEE International Conference on Information and Automation (ICIA)* (July 2017), pp. 517–522. 3, 7

[ARE*14] AGNER S. C., ROSEN M. A., ENGLANDER S., TOMASZEWSKI J. E., FELDMAN M. D., ZHANG P., MIES C., SCHNALL M. D., MADABHUSHI A.: Computerized image analysis for identifying triple-negative breast cancers and differentiating them from other molecular subtypes of breast cancer on dynamic contrast-enhanced MR images: A feasibility study. *Radiology 272*, 1 (2014), 91–99. doi:10.1148/radiol.14121031. 2

[ASL*11] AGNER S. C., SOMAN S., LIBFELD E., MCDONALD M., THOMAS K., ENGLANDER S., ROSEN M. A., CHIN D., NOSHER J., MADABHUSHI A.: Textural kinetics: A novel dynamic contrast-enhanced (DCE)-MRI feature for breast lesion classification. *J Digit Imaging 24*, 3 (June 2011), 446–463. doi:10.1007/s10278-010-9298-1. 1

[BFB*09] BALTZER P. A. T., FREIBERG C., BEGER S., VAG T., DIETZEL M., HERZOG A. B., GAJDA M., CAMARA O., KAISER W. A.: Clinical MR-mammography: are computer-assisted methods superior to visual or manual measurements for curve type analysis? a systematic approach. *Acad Radiol 16*, 9 (Sept. 2009), 1070–1076. doi:10.1016/j.acra.2009.03.017. 1, 2

[BFS*18] BRAY F., FERLAY J., SOERJOMATARAM I., SIEGEL R. L., TORRE L. A., JEMAL A.: Global cancer statistics 2018: GLOBOCAN estimates of incidence and mortality worldwide for 36 cancers in 185 countries. *CA: A Cancer Journal for Clinicians 68*, 6 (2018), 394–424. doi:10.3322/caac.21492. 1

[BHH03] BREWER C. A., HATCHARD G. W., HARROWER M. A.: ColorBrewer in Print: A Catalog of Color Schemes for Maps. *Cartogr Geogr Inf Sci 30*, 1 (Jan. 2003), 5–32. doi:10.1559/152304003100010929. 5

[BJGG*03] BAR-JOSEPH Z., GERBER G. K., GIFFORD D. K., JAAKKOLA T. S., SIMON I.: Continuous representations of time-series gene expression data. *J Comput Biol 10*, 3 (June 2003), 341–356. doi:10.1089/10665270360688057. 4

[BK07] BIRANT D., KUT A.: ST-DBSCAN: An algorithm for clustering spatial–temporal data. *Data & Knowledge Engineering 60*, 1 (Jan. 2007), 208–221. doi:10.1016/j.datak.2006.01.013. 3

[BLA*07] BEHRENS S., LAUE H., ALTHAUS M., BOEHLER T., KUEMMERLEN B., HAHN H. K., PEITGEN H.-O.: Computer assistance for MR based diagnosis of breast cancer: Present and future challenges. *Comput Med Imaging Graph 31*, 4 (June 2007), 236–247. doi:10.1016/j.compmedimag.2007.02.007. 1

[BSB*09] BURNSIDE E. S., SICKLES E. A., BASSETT L. W., RUBIN D. L., LEE C. H., IKEDA D. M., MENDELSON E. B., WILCOX P. A., BUTLER P. F., D'ORSI C. J.: The ACR BI-RADS Experience: Learning From History. *J Am Coll Radiol 6*, 12 (Dec. 2009), 851–860. doi:10.1016/j.jacr.2009.07.023. 1

[CNZ*12] CHEN X., NIEMEIJER M., ZHANG L., LEE K., ABRAMOFF M. D., SONKA M.: Three-Dimensional Segmentation of Fluid-Associated Abnormalities in Retinal OCT: Probability Constrained Graph-Search-Graph-Cut. *IEEE Trans Med Imaging 31*, 8 (Aug. 2012), 1521–1531. doi:10.1109/TMI.2012.2191302. 2, 4

[DGV*16] DALMIŞ M. U., GUBERN-MÉRIDA A., VREEMANN S., KARSSEMEIJER N., MANN R., PLATEL B.: A computer-aided diagnosis system for breast DCE-MRI at high spatiotemporal resolution. *Med Phys 43*, 1 (Jan. 2016), 84–94. doi:10.1118/1.4937787. 1

[DVK*18] DALMIŞ M. U., VREEMANN S., KOOI T., MANN R. M., KARSSEMEIJER N., GUBERN-MÉRIDA A.: Fully automated detection of breast cancer in screening MRI using convolutional neural networks. *J Med Imaging 5*, 1 (Jan. 2018). doi:10.1117/1.JMI.5.1.014502. 1

[FB14] FISCHER U., BAUM F.: *Diagnostik und Therapie des Mammakarzinoms*. Georg Thieme Verlag, Jan. 2014. 7

[FGKD01] FURMAN-HARAN E., GROBGELD D., KELCZ F., DEGANI H.: Critical role of spatial resolution in dynamic contrast-enhanced breast MRI. *J Magn Reson Imaging 13*, 6 (June 2001), 862–867. doi:10.1002/jmri.1123. 2, 4

[FKG99] FISCHER U., KOPKA L., GRABBE E.: Breast Carcinoma: Effect of Preoperative Contrast-enhanced MR Imaging on the Therapeutic Approach. *Radiology 213*, 3 (Dec. 1999), 881–888. doi:10.1148/radiology.213.3.r99dc01881. 1

[FWR*17] FEDERICO P., WAGNER M., RIND A., AMOR-AMORÓS A., MIKSCH S., AIGNER W.: The role of explicit knowledge: A conceptual model of knowledge-assisted visual analytics. In *Proc. of IEEE VAST* (Oct. 2017), pp. 92–103. doi:10.1109/VAST.2017.8585498. 7

[GNPS13] GLASSER S., NIEMANN U., PREIM B., SPILIOPOULOU M.: Can we distinguish between benign and malignant breast tumors in DCE-MRI by studying a tumor's most suspect region only? In *Proc. of International Symposium on Computer-Based Medical Systems* (2013), pp. 77–82. doi:10.1109/CBMS.2013.6627768. 3

[GPTP10] GLASSER S., PREIM U., TÖNNIES K., PREIM B.: A visual analytics approach to diagnosis of breast DCE-MRI data. *Comput Graph 34*, 5 (Oct. 2010), 602–611. doi:10.1016/j.cag.2010.05.016. 2, 3

[HHHV01] HIEKEN T. J., HARRISON J., HERREROS J., VELASCO J. M.: Correlating sonography, mammography, and pathology in the assessment of breast cancer size. *The American Journal of Surgery 182*, 4 (Oct. 2001), 351–354. doi:10.1016/S0002-9610(01)00726-7. 2

[HKvH08] HEMMER J. M., KELDER J. C., VAN HEESEWIJK H. P. M.: Stereotactic large-core needle breast biopsy: analysis of pain and discomfort related to the biopsy procedure. *Eur Radiol 18*, 2 (Feb. 2008), 351–354. doi:10.1007/s00330-007-0762-3. 1

[IFDS16] IORIO C., FRASSO G., D'AMBROSIO A., SICILIANO R.: Parsimonious time series clustering using P-splines. *Expert Syst Appl 52*, Supplement C (June 2016), 26–38. doi:10.1016/j.eswa.2016.01.004. 3

[KKSZ11] KRIEGEL H.-P., KRÖGER P., SANDER J., ZIMEK A.: Density-based clustering. *Data Min Knowl Discov 1*, 3 (2011), 231–240. doi:10.1002/widm.30. 3

[KMK*99] KUHL C. K., MIELCARECK P., KLASCHIK S., LEUTNER C., WARDELMANN E., GIESEKE J., SCHILD H. H.: Dynamic breast MR imaging: Are signal intensity time course data useful for differential diagnosis of enhancing lesions? *Radiology 211*, 1 (Apr. 1999), 101–110. doi:10.1148/radiology.211.1.r99ap38101. 2

[Kuh07] KUHL C.: The Current Status of Breast MR Imaging Part I. Choice of Technique, Image Interpretation, Diagnostic Accuracy, and Transfer to Clinical Practice. *Radiology 244*, 2 (2007), 356–378. doi:10.1148/radiol.2442051620. 2

[MBB*17] MUS R. D., BORELLI C., BULT P., WEILAND E., KARSSEMEIJER N., BARENTSZ J. O., GUBERN-MÉRIDA A., PLATEL B., MANN R. M.: Time to enhancement derived from ultrafast breast MRI as a novel parameter to discriminate benign from malignant breast lesions. *Eur J Radiol 89* (Apr. 2017), 90–96. doi:10.1016/j.ejrad.2017.01.020. 1

[MCW*16] MARINO M. A., CLAUSER P., WOITEK R., WENGERT G. J., KAPETAS P., BERNATHOVA M., PINKER-DOMENIG K., HELBICH T. H., PREIDLER K., BALTZER P. A. T.: A simple scoring system for breast MRI interpretation: does it compensate for reader experience? *Eur Radiol 26*, 8 (Aug. 2016), 2529–2537. doi:10.1007/s00330-015-4075-7. 1

[MDvP17] MILENKOVIĆ J., DALMIŞ M. U., ŽGAJNAR J., PLATEL B.: Textural analysis of early-phase spatiotemporal changes in contrast enhancement of breast lesions imaged with an ultrafast DCE-MRI protocol. *Med Phys 44*, 9 (Sept. 2017), 4652–4664. doi:10.1002/mp.12408. 1

[MF15] MIRANDA G. H. B., FELIPE J. C.: Computer-aided diagnosis system based on fuzzy logic for breast cancer categorization. *Computers in Biology and Medicine 64* (Sept. 2015), 334–346. doi:10.1016/j.compbiomed.2014.10.006. 3, 7

[MK16] M.K V., K K.: A Survey on Similarity Measures in Text Mining. *Machine Learning and Applications: An International Journal 3*, 1 (Mar. 2016), 19–28. doi:10.5121/mlaij.2016.3103. 6

[MMSJP99] MEYER S., MÜLLER-SCHIMPFLE M., JÜRGENS H., PEITGEN H.: MT-DYNA: Computer assistance for the evaluation of dynamic MR and CT data in a clinical environment. In *Proc. of Computer Assisted Radiology and Surgery* (1999), pp. 331–334. 1

[MPF*17] MARRONE S., PIANTADOSI G., FUSCO R., PETRILLO A., SANSONE M., SANSONE C.: An Investigation of Deep Learning for Lesions Malignancy Classification in Breast DCE-MRI. In *Image Analysis and Processing* (2017), Lecture Notes in Computer Science, Springer International Publishing, pp. 479–489. doi:10.1007/978-3-319-68548-9_44. 2

[Nat18] NATIONAL GUIDELINE ALLIANCE (UK): *Early and locally advanced breast cancer: diagnosis and management*. National Institute for Health and Care Excellence: Clinical Guidelines. National Institute for Health and Care Excellence (UK), London, 2018. 1

[ODH*07] OELTZE S., DOLEISCH H., HAUSER H., MUIGG P., PREIM B.: Interactive Visual Analysis of Perfusion Data. *IEEE Trans Vis Comput Graph 13*, 6 (Nov. 2007), 1392–1399. doi:10.1109/TVCG.2007.70569. 2

[PMW*14] PLATEL B., MUS R., WELTE T., KARSSEMEIJER N., MANN R.: Automated characterization of breast lesions imaged with an ultrafast DCE-MR protocol. *IEEE Trans Med Imaging 33*, 2 (Feb. 2014), 225–232. doi:10.1109/TMI.2013.2281984. 2

[POM*09] PREIM B., OELTZE S., MLEJNEK M., GROLLER E., HENNEMUTH A., BEHRENS S.: Survey of the Visual Exploration and Analysis of Perfusion Data. *IEEE Trans Vis Comput Graph 15*, 2 (Mar. 2009), 205–220. doi:10.1109/TVCG.2008.95. 2

[PPA*13] PATWARY M. A., PALSETIA D., AGRAWAL A., LIAO W.-K., MANNE F., CHOUDHARY A.: Scalable parallel OPTICS data clustering using graph algorithmic techniques. In *Proc. SC: The International Conference for High Performance Computing, Networking, Storage, and Analysis* (2013), pp. 49:1–49:12. doi:10.1145/2503210.2503255. 3, 4, 5

[Pri57] PRIM R. C.: Shortest connection networks and some generalizations. *Bell System Technical Journal 36*, 6 (Nov. 1957), 1389–1401. 5

[RPP*20] ROMEO V., PICARIELLO V., PIGNATA A., MANCUSI V., STANZIONE A., CUOCOLO R., DI CRESCENZO R., ACCURSO A., STAIBANO S., IMBRIACO M.: Influence of different post-contrast time points on dynamic contrast-enhanced (DCE) MRI T staging in breast cancer. *Eur J Radiol 124* (Mar. 2020), 108819. doi:10.1016/j.ejrad.2020.108819. 1

[RTP17] RASTI R., TESHNEHLAB M., PHUNG S. L.: Breast cancer diagnosis in DCE-MRI using mixture ensemble of convolutional neural networks. *Pattern Recognition 72* (Dec. 2017), 381–390. doi:10.1016/j.patcog.2017.08.004. 3

[RV18] RADA-VILELA J.: The fuzzylite libraries for fuzzy logic control, 2018. Accessed 2020/01/10. URL: https://fuzzylite.com/. 7

[SAea17] SARDANELLI F., AASE H. S., ET AL.: Position paper on screening for breast cancer by the European Society of Breast Imaging (EUSOBI) and 30 national breast radiology bodies. *Eur Radiol 27*, 7 (July 2017). doi:10.1007/s00330-016-4612-z. 1

[SG11] SUN Y., GENTON M. G.: Functional boxplots. *J Comput Graph Stat 20*, 2 (Jan. 2011), 316–334. doi:10.1198/jcgs.2011.09224. 3, 5

[TGVB13] TANG M., GORELICK L., VEKSLER O., BOYKOV Y.: GrabCut in one cut. In *Proc. of ICCV* (Dec. 2013), pp. 1769–1776. doi:10.1109/ICCV.2013.222. 2, 4

[WAJ*18] WÖCKEL A., ALBERT U.-S., JANNI W., SCHARL A., KREIENBERG R., STÜBER T.: The Screening, Diagnosis, Treatment, and Follow-Up of Breast Cancer. *Deutsches Ärzteblatt International 115*, 18 (May 2018), 316–323. doi:10.3238/arztebl.2018.0316. 1

[ZLD*19] ZHOU J., LUO L.-Y., DOU Q., CHEN H., CHEN C., LI G.-J., JIANG Z.-F., HENG P.-A.: Weakly supervised 3d deep learning for breast cancer classification and localization of the lesions in MR images. *Journal of Magnetic Resonance Imaging 50*, 4 (2019), 1144–1151. doi:10.1002/jmri.26721. 2, 3